Modeling of volume change phenomena in a Li−air battery

CrossMark

Kisoo Yoo, Soumik Banerjee, Prashanta Dutta*

School of Mechanical and Materials Engineering, Washington State University, Pullman, WA 99164-2920, USA

HIGHLIGHTS

- A mathematical model is developed considering the effective volume changes for a lithium−air battery.
- Moving boundary technique is used to obtain mathematical model.
- The volume change significantly affects the electrical performance of lithium−air cell.
- Insoluble lithium peroxide can cause electrolyte leakage, and this leakage worsens at lower current density.

ABSTRACT

Volume change can occur in a lithium−air cell due to Li metal oxidation (reduction) in anode during discharge (charge) and due to solubility of reaction product (lithium peroxide) in the electrolyte at cathode. A mathematical model is developed to study the performance of lithium−air batteries considering the significant volume changes at the anode and cathode sides. Moving boundary technique is used to obtain the governing equations for transport of lithium ions and oxygen as well as for liquid phase potential. A numerical method is introduced to solve the moving boundary problem, and the electrical performance of lithium−air cell is obtained for various load conditions. Results obtained from this model are validated with experimental results for Lithium−air cell. Numerical results indicate that volume changes significantly affect the functioning of lithium−air cells. The high solubility of lithium peroxide in the electrolyte can reduce the passivation in the cathode, but it can also reduce the effective reaction area in the anode. However, the benefit of the former outweighs the detriment of the later phenomenon. On the other hand, if lithium peroxide is insoluble in electrolyte, electrolyte leakage can take place due to decrease in total available space for electrolyte.

© 2014 Elsevier B.V. All rights reserved.

1. Introduction

Based on ever-growing societal demand for stable energy supply, recent times have witnessed an increasing emphasis on developing energy storage devices such as fuel cells, batteries, supercapacitors, etc. Among the myriad options, the lithium battery is expected to play a dominant role because of its higher specific energy and specific power. During the last decade, Li-ion batteries have revolutionized the portable and consumer electronics market. However, even when fully developed, the highest energy storage achieved by a state-of-the-art Li-ion battery is too low to meet current demands in the automotive industry [1]. Moreover, there is an increasing demand for light weight and high capacity batteries for power hungry consumer electronics. Li−air batteries [2,3],

which are based on Li anode and air cathode, have greater theoretical energy densities and have been proposed as an alternative for electric vehicles and hybrid electric vehicles.

The theoretical specific energy of Li−air battery is as high as gasoline, if the weight of oxygen and cathode materials is not considered in calculation [3]. Bruce et al. [4] has reported a specific energy of 3505 Wh kg^{-1} considering the weight of lithium peroxide (Li$_2$O$_2$) at the end of the discharge. This specific energy is 3.25 times smaller than the ideal case where the weight of oxygen is not accounted for. Girishkumar et al. [3] has estimated the specific energy (gravimetric energy density) of lithium−air battery based on the performance of Zn−air battery, and they used a factor to relate theoretical energy density with the practical one. The factor used for zinc-air was 0.4−0.5, but a much lower value (factor = 0.145) was used for the estimation of actual energy density for lithium−air battery considering the ultra-light weight of lithium [3].

Numerical modeling can assist in predicting the performance of a lithium−air battery considering the role of anode, cathode and

* Corresponding author.
   E-mail address: prashanta@wsu.edu (P. Dutta).

separator. Models can also identify the potential roadblocks and provide direction for a highly efficient battery. The physical and mathematical models for Li–air battery are very similar to that for Li-ion battery, except one has to consider the transport of oxygen in lithium–air battery. Therefore, a model for Li–air batteries can be developed based on that of Li-ion batteries. Several models for lithium-ion batteries have been reported in the literature [5–7]. The transport phenomena in a lithium-ion battery are presented in the seminal work of Newman [8], where a mathematical model was developed for species transport in concentrated binary electrolytes. In addition, important theory for transport in porous electrodes [9] was developed which was widely used to model lithium-ion batteries [5,6,10].

In recent years, couple of models was developed for Li–air batteries. Sandhu et al. [11] have modeled the porous cathode region of a lithium–air battery as cylindrical pores, and studied the performance of the Li–air battery considering the blockage of pore due to the Li_2O_2 deposition. On the other hand, Sahapatsombut et al. [12] developed model equations for transport through Li_2O_2 layer in the porous cathode, and studied the effects of oxygen and Li_2O_2 solubility in electrolytes for lithium–air batteries. Aforementioned models were introduced to address issues in cathodes such as pore plugging, electric passivation, etc. However, these models do not capture the important volume change phenomena on the anode side.

Like cathode side, significant volume change can take place in the anode side of lithium batteries [13]. The existing lithium-ion battery anode is mainly based on lithium metal intercalated on graphite. Although graphite provides an excellent support system for anodic lithium, it contributes to the weight of the battery reducing the effective specific capacity. To improve the specific capacity, lithium metal alloy such as lithium-tin (Li–Sn) is suggested as anode material [14]. However, Li–Sn alloy anode is not very useful for lithium batteries due to significant volume change, which introduces large mechanical stress in the system [15]. Recently, Li metal foil is introduced as anode material to reduce the battery weight furthermore. Similar to the lithium metal alloy anode, significant volume change occurs in lithium metal anode due to oxidation and reduction. Visco et al. [16] proposed a mechanical stacking method to maintain constant contact between separator and metallic anode. However, there are two issues with this stacking mechanism. First, the supporting system used for cell stacking will add to the battery weight reducing the effective specific capacity significantly. Second, the stacking pressure induced mechanical stress has a higher probability of damaging the thin lithium foil anode in lithium–air battery; the cyclic charging and discharging will worsen the problem causing frequent mechanical failure [14]. Aforementioned drawbacks could be circumvented in lithium–air batteries by allowing the lithium anode interface to move freely during charging and discharging. However, there is no mathematical or numerical model to predict the performance of lithium–air batteries, when the anode interface is free to move due to oxidation and reduction. In this study, a mathematical model is developed to account for the movement of anode interface during charge and discharge using moving boundary method. An in house numerical tool is developed to study the electrochemical performance of Li–air batteries considering volume change due to moving interface of the anode as well as the solubility of reaction product in the cathode during charge and discharge operations.

2. Model

2.1. Model system

A lithium air cell primarily consists of an anode, a separator and a cathode as shown in Fig. 1. Lithium metal is generally used as

anode, while porous materials are used as separator and cathode. A solid polymer having negligible electric conductivity is used as separator to prevent battery from internal short. On the other hand, carbon or catalyst loaded carbon is generally used as cathode such that it can conduct electricity. The porous area in both separator and cathode are filled with organic electrolyte; lithium ion and oxygen are transported through the electrolyte.

In lithium–air batteries, the oxygen is supplied from the atmospheric air. The gas diffusion layer (GDL) provides passage for oxygen transport to the cathode reaction sites, but it prevents electrolyte leakage from the cathode side. In this study, the computational domain ranges from the anode interface ($x = -\delta(t)$) to the end of cathode ($x = L_{sp} + L_c$). In our macroscopic model, anode protective layer (APL) or solid electrolyte interphase (SEI) was not considered in the computational domain because it is ultra-thin (less than dozens of nanometer) compare to anode and cathode regions [12,18]. However, the effect of SEI is considered in estimating the transfer current density. We specifically studied the performance of a single lithium–air cell neglecting the mechanical constraints or stack pressure due to the reasons explained before. In other words, it is assumed that the anode reaction interface is free to move due to Li metal oxidation (reduction) during discharge (charge).

2.2. Chemical reaction

In this section, we review the general chemistry for a lithium–air cell (Fig. 1) during discharge stage. Li metal gets oxidized in the anode by losing an electron as

$$Li \rightarrow Li^+ + e^-. \tag{1}$$
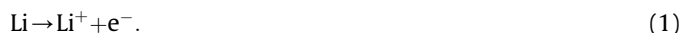
This reaction happens at the free surface, and Li ion is transferred to electrolyte through SEI. The electron, released from Li metal, moves to cathode through the outer loop, while the lithium ion transports to cathode via electrolyte. At cathode, oxygen from air gets reduced in presence of lithium ions and electrons as [4]

$$O_2 + e^- \rightarrow O_2^- \tag{2a}$$

$$O_2^- + Li^+ \rightarrow LiO_2 \tag{2b}$$

$$2LiO_2 \rightarrow Li_2O_2 + O_2. \tag{2c}$$

The lithium peroxide (Li_2O_2) is generally insoluble in electrolyte and it can adversely affect the performance of lithium–air cell by covering the active area of cathode materials [19]. Lithium peroxide can undergo further reduction to form Li_2O as

$$Li_2O_2 + 2Li^+ + 2e^- \rightarrow 2Li_2O. \tag{2d}$$

However, conversion from lithium peroxide to Li_2O is not very common. Thus, in this study, the overall cathode reaction is derived from the reaction pathway shown in equation 2(a–c) as

$$2Li^+ + O_2 + e^- \rightarrow Li_2O_2. \tag{2e}$$

To model the charging process, the anodic (1) and cathodic (2e) reactions are reversed.

2.3. Mathematical model for lithium–air cell

In a galvanic cell such as lithium–air cell, the reaction rates at the anode and cathode side depend on the corresponding surface overpotential. The local transfer current density at the reaction sites can be calculated using the Butler–Volmer Equation as [12]
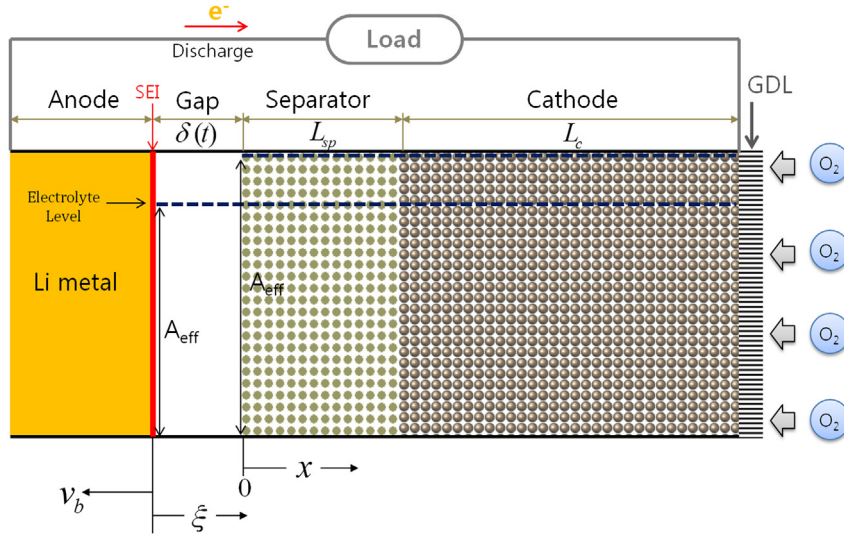
Fig. 1. Model domain for a Li–air battery indicating lithium anode, solid electrolyte interface, gap, porous separator and cathode. A gap ($\delta(t)$) is created between the separator and lithium anode due to the movement of anode interface during discharge, which is filled with liquid electrolyte. Here x and ξ are the fixed and moving coordinate system. The computational domain ranges from $x = -\delta(t)$ to $x = L_{in} = L_c + L_{sp}$. During discharge, current is supplied by the battery, and the I_{load} is positive. On the other hand, during charge current is applied to the battery, and the I_{load} is negative.

$$\text{Anode}: \quad j_a = i_0\left[\exp\left(\frac{(1-\beta)nF}{RT}\eta_a\right) - \exp\left(\frac{-\beta nF}{RT}\eta_a\right)\right] \quad (3)$$

$$\text{Cathode}: \quad j_c = nF\left\{k_a C_{Li_2O_2}\exp\left(\frac{(1-\beta)nF}{RT}\eta_c\right) - k_c(C_{Li^+})^2 C_{O_2}\exp\left(\frac{-\beta nF}{RT}\eta_c\right)\right\} \quad (4)$$

where i_0 is the current density coefficient and it is calculated from experiential data. Here β is the symmetry factor, R is the gas constant, T is the operating temperature, n is the number of electron transferred, and F is the Faraday constant. C_{Li^+}, C_{O_2}, and $C_{Li_2O_2}$ are concentrations of Li ion, oxygen, and lithium peroxide, respectively; k_a and k_c are reaction rate constants at the anode and cathode, respectively. The overpotential at the anode (η_a) and cathode (η_c) reaction sites can be given as:

$$\eta_a = \phi_s - \phi_l - E_a^0 \quad (5a)$$

$$\eta_c = \phi_s - \phi_l - \Delta\phi_{film} - E_c^0 \quad (5b)$$

where $\Delta\phi_{film}$ is potential drop across lithium peroxide film, ϕ_s and ϕ_l are solid and liquid phase potential, respectively, and E_a^0 and E_c^0 are theoretical open circuit potential at the anode and cathode, respectively. Thus, in order to calculate the local current density, one has to calculate C_{Li^+}, C_{O_2}, $C_{Li_2O_2}$, ϕ_s, and ϕ_l.

In a lithium–air cell, the Li ion concentration is usually much higher than 1 M. Hence, the Nernst–Planck equation cannot be used to predict the lithium ion concentration in the electrolyte. In a concentrated solution, the concentration of ionic components can be obtained as [8]

$$\frac{\partial(\varepsilon C_{Li^+})}{\partial t} = \nabla\cdot\left(D_{eff,\,Li^+}\nabla C_{Li^+}\right) - \frac{\nabla\left(t_+^0\,\vec{i_l}\right)}{z_+\nu_+ F} + S_{Li^+} \quad (6)$$

where t_+^0, $\vec{i_l}$, z_+, and ν_+ are the transference number, current in liquid phase, charge number, and reaction stoichiometric

coefficient of lithium ion, respectively, ε is the porosity in the separator and cathode. The porosity is constant in separator, but varies in cathode area depending on the deposition of Li_2O_2. $D_{eff,Li}$ is the effective diffusivity of Li ion which is calculated using Burggeman correlation [20] as

$$D_{eff,Li^+} = D_{Li^+}\varepsilon^{1.5} \quad (7a)$$

where D_{Li^+} is the Li ion diffusivity, and in concentrated solution it varies with Li ion concentration and chemical activity as [8].

$$D_{Li^+} = \frac{(z_+ - z_-)D_{+0}D_{-0}}{z_+ D_{+0} - z_- D_{-0}}\frac{C_T}{C_0}\left[1 - \frac{d(\ln C_0)}{d(\ln C_{Li^+})}\right]\left[1 + \frac{d(\ln f_\pm)}{d(\ln C_{Li^+})}\right] \quad (7b)$$

where $f_\pm$ is the chemical activity coefficient. The source (sink) term in the lithium ion mass conservation equation can be calculated from

$$S_{Li^+} = \frac{aj_i}{z_+\nu_+ F} \quad (8)$$

where the subscript i is the index to identify anode or cathode and a is the specific area. For discharge case, S_{Li^+} will be a source term for anode side, but it will act as a sink for cathode side. During the charge state, S_{Li^+} will be a sink term for anode side and it will act as a source for cathode side since reduction reaction happens at anode side while oxidation reaction takes place in cathode.

In a typical lithium–air cell, the concentration of oxygen in electrolyte is quite low (a few mM) owing to the low solubility, and dilute solution assumption can be used for the mass conservation equation of oxygen. Thus, in an organic electrolyte, the concentration of oxygen can be obtained as [12]

$$\frac{\partial(\varepsilon C_{O_2})}{\partial t} = \nabla\cdot\left(D_{eff,O_2}\nabla C_{O_2}\right) + S_{O_2} \quad (9)$$

where D_{eff,O_2} is the effective diffusivity of oxygen, and for porous media it is calculated using Burggeman correlation as

$$D_{eff,O_2} = D_{O_2}\varepsilon^{1.5} \quad (10)$$

The last tem in equation (9) presents source/sink term, and it can be given as

$$S_{O_2} = \frac{aj_c}{z_+ \nu_+ F} \tag{11}$$

In a lithium–air battery, oxygen is consumed in cathode during discharge state but regenerated during charge state.

The mass conservation equation for Li_2O_2 can be obtained by balancing the transient term with the source tem as

$$\frac{\partial(C_{Li_2O_2})}{\partial t} = -\frac{aj_c}{nF} \tag{12}$$

Here the diffusion term is not considered since the Li_2O_2 is generally insoluble in an organic electrolyte. In a lithium–air battery, Li_2O_2 fills the cathode void area during the discharge state. Therefore, cathode porosity can be obtained by subtracting the space taken by Li_2O_2 from initial cathode porous area (ε^0) as

$$\varepsilon = \varepsilon^0 - C_{Li_2O_2} \cdot \frac{M_{Li_2O_2}}{\rho_{Li_2O_2}} \tag{13}$$

where $M_{Li_2O_2}$ and $\rho_{Li_2O_2}$ are molecular weight and the mass density of Li_2O_2, respectively.

The electric potential in a lithium–air cell can be divided into two parts: solid phase potential (ϕ_s) and liquid phase potential (ϕ_l). Solid phase potential is only present in the solid regions of cathode materials, while the liquid phase potential is related to electrolyte, and it exists throughout the computational domain. The former potential can be obtained from charge conservation in the cathodic solid as:

$$\nabla \cdot \left(\sigma_{\mathrm{eff}} \nabla \varphi_s \right) = aj_c \tag{14}$$

where σ_{eff} is electric conductivity of cathode material, and for porous cathode it is calculated using Burggeman correlation.

$$\sigma_{\mathrm{eff}} = \sigma(1 - \varepsilon)^{1.5} \tag{15}$$

Liquid phase electric potential equation is more intricate because of Li ion movement in concentrated solution. Newman has derived an equation for liquid phase electric potential from the Gibbs–Duhem relation as [8]

$$\nabla \cdot \left(\kappa_{\mathrm{eff}} \nabla \varphi_l \right) = \nabla \cdot \left\{ \frac{2\kappa_{\mathrm{eff}} RT}{F} \left(1 - t_+^0 \right) \left[1 + \frac{d(\ln f_\pm)}{d(\ln C_{Li^+})} \right] \frac{1}{C_{Li^+}} \nabla C_{Li^+} \right\} - aj_c \tag{16}$$

where κ_{eff} is the effective ionic conductivity of Li ion in electrolyte, and for porous media it can be expressed as

$$\kappa_{\mathrm{eff}} = \kappa \varepsilon^{1.5} \tag{17a}$$

where κ is the ionic conductivity of electrolyte and it varies with Li ion concentration as

$$\frac{1}{\kappa} = -\frac{RT}{C_T z_+ z_- F^2} \left(\frac{1}{D_{+-}} + \frac{C_0}{C_+} \frac{1}{D_{0-}} t_-^0 \right). \tag{17b}$$

here, C_T is total mole concentration of solution and D_{+-}, and D_{0-} are diffusion coefficients for interaction of cations-anions and neutral solvent-anions, respectively.

3. Model for moving boundary

3.1. Anode interface velocity

During discharge lithium metal gets oxidized to form lithium ions. These lithium ions dissolve in the adjacent electrolyte, which results in a change in space between the separator and the anode interface. Fig. 2(a) shows the interface location of Li anode at the beginning of discharge and at an instant t indicating a change in volume of $\Delta V = \delta(t)A$, where $\delta(t)$ is the length between anode interface and separator and A is the anode surface area. This volume change in the anode side depends on the applied load, and it can be given as

$$\Delta V = \frac{M_{Li}}{\rho_{Li}} \int_0^T \frac{I_{\mathrm{load}} A}{\nu_{Li} F} dt \tag{18}$$

where M_{Li}, ρ_{Li}, ν_{Li} are molecular weight, density, and stoichiometric coefficient for lithium, respectively, and I_{load} is the applied current density. Using equation (18), anode boundary velocity (ν_b) and total displacement (δ_T) can be obtained as
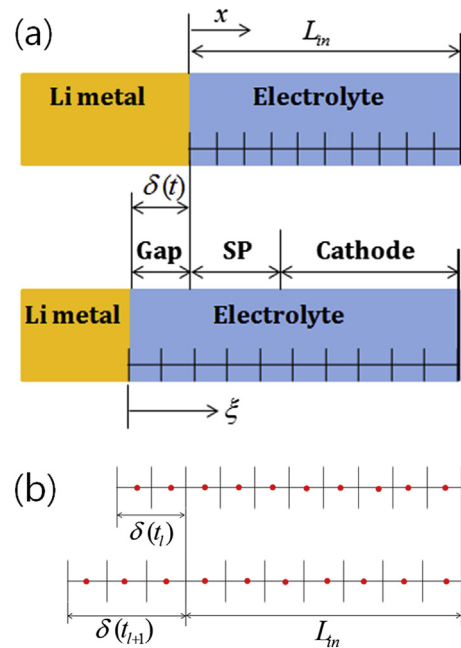
$$\nu_b = \frac{M_{Li} I_{\mathrm{load}}}{\nu_{Li} \rho_{Li} F} \tag{19a}$$

$$\delta_T = \delta(t = T) = \frac{M_{Li}}{\nu_{Li} \rho_{Li} F} \int_0^T (I_{\mathrm{load}}) dt \tag{19b}$$

where T is the final time.

3.2. Governing equations for moving mesh

The movement of anode interface affects the species concentration profile and liquid phase electric potential. This phenomenon

Fig. 2. (a) Schematics of the 1D computational domain at the beginning of discharge and at any instant of time t. Here SP stands for separator. (b) Computational grids are stretched by movement of solid anode boundary. The boundary velocity depends on current density.

is very similar to melting of a solid. Thus, a moving boundary technique can be used to obtain the governing equations for pertinent variables. Here it is assumed that the electrolyte occupies the gap between the anode interface and the separator. To obtain governing equations for moving boundary problem, a moving co-ordinate is introduced. The origin of the moving coordinate (ξ) is at the reaction interface of the anode metal (Li) as shown in Fig. 2(a). Thus, governing equation for moving coordinate can be obtained using coordinate transformation technique [21]. If the origin of fixed coordinate system (x) is located at the initial lithium–electrolyte interface position, the relation between moving and fixed coordinate can be given as

$$\xi = x + \int_0^t \alpha(x,t)dt \tag{20a}$$

where $\alpha(x, t)$ is the velocity of the grid points in moving coordinate system, and it can be given as

$$\alpha(x,t) = v_b\left[1 - \frac{x+\delta}{\delta_t}\right]. \tag{20b}$$

Here δ is the length of the electrolyte region at any instant t, and it consists of separator (L_{sp}), cathode region (L_c) and space due to boundary movement (δ) as

$$\delta_t = \delta + L_{sp} + L_c \tag{21}$$

Using equations (20a) and (20b), the temporal and spatial derivative terms can be rewritten as

$$\frac{\partial}{\partial t} = \frac{\partial}{\partial t} + v_b\left(1 - \frac{\xi - \alpha t + \delta}{\delta_t}\right)\frac{\partial}{\partial \xi} \tag{22a}$$

$$\frac{\partial}{\partial x} = \left(1 - \frac{v_b}{\delta_t}\right)\frac{\partial}{\partial \xi} \tag{22b}$$

Thus the governing equations for Li ion and oxygen in the moving coordinate system become

$$\frac{\partial\left(\varepsilon C_{Li^+}^*\right)}{\partial t} + v_b\left(1 - \frac{\xi - \alpha t + \delta}{\delta_t}\right)\frac{\partial\left(\varepsilon C_{Li^+}^*\right)}{\partial \xi}$$
$$= \left(1 - \frac{v_b}{\delta_t}\right)\frac{\partial}{\partial \xi}\left[D_{Li^+,eff}\left(1 - \frac{v_b}{\delta_t}\right)\frac{\partial C_{Li^+}^*}{\partial \xi}\right] + \left(1 - \frac{v_b}{\delta_t}\right)\frac{\partial}{\partial \xi}\left(\frac{i_{l,x}^* t_+}{F}\right) + S_{Li^+}^* \tag{23}$$

$$\frac{\partial\left(\varepsilon C_{O_2}^*\right)}{\partial t} + v_b\left(1 - \frac{\xi - \alpha t + \delta}{\delta_t}\right)\frac{\partial\left(\varepsilon C_{O_2}^*\right)}{\partial \xi}$$
$$= \left(1 - \frac{v_b}{\delta_t}\right)\frac{\partial}{\partial \xi}\left[D_{Li^+,eff}\left(1 - \frac{v_b}{\delta_t}\right)\frac{\partial C_{O_2}^*}{\partial \xi}\right] + S_{O_2}^* \tag{24}$$

Similarly, the liquid phase electric potential in the moving coordinate can be obtained as

Here superscript * means that the value is in moving coordinate system. The source terms in the moving boundary systems (j_c^*, $S_{Li^+}^*$ and $S_{O_2}^*$) should be obtained from variables mapping between fixed and moving coordinate which are presented in Section 3.5. Governing equations for Li_2O_2 concentration and solid phase potential are not obtained for the moving coordinate system since they will only be solved in the cathode region from equations (12) and (14).

3.3. Electrolyte space

Initially electrolyte fills all the porous (void) space in the separator and cathode side. During discharge, the available space for electrolyte changes in both anode and cathode sides. As mentioned earlier, in the anodic side, space is created for electrolyte due to the movement of anode interface. On the other hand, in the cathode side, the room available for electrolyte decreases due to the deposition of Li_2O_2 in the porous area. The total available space for electrolyte can be calculated as

$$V(t) = A\left[\delta(t) + \varepsilon_{sp}L_{sp} + \int_{L_{sp}}^{L_{sp}+L_c}\varepsilon_c(t)dx\right] \tag{26}$$

where subscripts sp and c mean separator and cathode, respectively. Thus the ratio between available volume to electrolyte volume (V_{el}) can be defined as

$$r = \frac{V(t)}{V_{el}}. \tag{27}$$

For an incompressible electrolyte, the electrolyte volume can be given as

$$V_{el} = A_{eff}(t)\left[\delta(t) + \varepsilon_{sp}L_{sp} + \int_{L_{sp}}^{L_{sp}+L_c}\varepsilon_c dx\right] \tag{28}$$

Here it is assumed that there is no surface tension or capillary effect between the electrolyte and the electrode materials. In other words, the electrolyte is considered completely settled due to gravity. Since the volume of electrolyte does not change with time, V_{el} can be calculated from equation (26) at time $t = 0$, and the effective surface area for reaction can be given as

$$A_{eff}(t) = \frac{A\left[\varepsilon_{sp}L_{sp} + \int_{L_{sp}}^{L_{sp}+L_c}\varepsilon_c(t=0)dx\right]}{\left[\delta(t) + \varepsilon_{sp}L_{sp} + \int_{L_{sp}}^{L_{sp}+L_c}\varepsilon_c(t)dx\right]} \tag{29}$$

Above equation indicates that the effective surface area for reaction is affected by volume change in the cathode side as well as in the anode side. If $A_{eff} < A$, the local transfer current density will increase at the reaction sites of anode and cathode for a particular load affecting the cell performance.

$$\left(1 - \frac{v_b}{\delta_t}\right)\frac{\partial}{\partial \xi}\left[\kappa\left(1 - \frac{v_b}{\delta_t}\right)\frac{\partial \varphi_l^*}{\partial \xi}\right] = \left(1 - \frac{v_b}{\delta_t}\right)\frac{\partial}{\partial \xi}\left\{\frac{2\kappa RT}{F}\left(1 - t_+^0\right)\left[1 + \frac{d(\ln f_\pm)}{d\left(\ln C_{Li^+}^*\right)}\right]\frac{1}{C_{Li^+}^*}\left(1 - \frac{v_b}{\delta_t}\right)\frac{\partial C_{Li^+}^*}{\partial \xi}\right\} - aj_c^* \tag{25}$$

3.4. Boundary conditions

The computational domain (Fig. 1) for lithium ion, oxygen and liquid phase electric potential equations ranges from the reaction interface of anode ($x = -\delta$) to the end of cathode ($x = L_{in}$). The solid phase electric potential is only computed in the cathode region ($L_{sp} \leq x \leq L_{in}$). Boundary conditions for all four governing equations are listed in Table 1. The mass flux for Li ion is determined from the applied current density at the moving boundary ($\xi = 0$) and a no mass flux condition is prescribed at the right boundary. On the other hand, mass flux for oxygen is zero at the moving boundary, but its value at the right boundary is calculated from the oxygen available in the atmosphere. Although oxygen is continually supplied from atmosphere, the mass flux at the right boundary also depends on the solubility of oxygen in the electrolyte. For liquid phase electric potential, the gradient of potential is calculated from the applied current density at the moving boundary and an insulating boundary condition is used at the right side.

Boundary conditions for the solid phase electric potential are prescribed at the left and right side of the cathode. In this study, electrical isolation condition is applied for left boundary because the left side of cathode is in contact with separator, which has negligible electric conductivity. On the right side, the cathode is connected with current collector. So, the solid phase electric potential gradient was calculated from the applied current density.

3.5. Grid generation

In this study, uniform grid is used to obtain discretized algebraic equations from governing equations (12), (14), (23)–(25). Since the anode interface moves to left (right) during discharge (charge), the length of the computational domain changes with time. Thus, if a fixed number of grids is used for discretization process, the length of a grid and position of grid points change with time. Fig. 2(b) shows the grid locations for two consecutive time steps. The new location of the moving boundary for a particular time ($l + 1$) can be calculated as

$$\delta(t_{l+1}) = \delta(t_l) + \frac{M_{Li} I_{load}^{t_{l+1/2}}}{\nu_{Li^+} \rho_{Li} F} \cdot (t_{l+1} - t_l) \tag{30}$$

where $\delta(t_l)$ is the location at time t_l and $I_{app}^{t_{l+1/2}}$ is the applied current density at $l + 1/2$ time step. Thus, for moving mesh, the grid length and grid location can be given as

$$\Delta\xi(t_{l+1}) = \frac{L_{in} + \delta(t_{l+1})}{N} \tag{31a}$$

$$\xi_j(t_{l+1}) = \frac{[L_{in} + \delta(t_{l+1})] \cdot (j - 1/2)}{N} \tag{31b}$$

where $\xi_j(t_{l+1})$ is position of jth finite volume in moving coordinate, N is the number of finite volumes, and L_{in} is the initial length filled

with electrolyte which includes separator and cathode region as shown in Fig. 2(a).

3.6. Parameter mapping

As mentioned earlier, equations (23)–(25) are solved in the moving boundary system, while the equations (12) and (14) are solved in the fixed coordinate. Since these equations are coupled, pertinent variables should be shared between the two coordinate systems. Here, variables are mapped between coordinates using piece-wise linear interpolation scheme [21] shown in Fig. 3. Φ_i and Ψ_j represent variables at ith finite volume in the fixed grid and at the jth finite volume in the moving grid. Using linear interpolation technique, the parameter mapping can be expressed as

$$\Phi_i = \frac{\omega_W \Psi_E + \omega_E \Psi_W}{\omega_W + \omega_E} \tag{32a}$$

$$\Psi_j = \frac{\gamma_W \Phi_E + \gamma_E \Phi_W}{\gamma_W + \gamma_E} \tag{32b}$$

where ω and γ are geometrical distance and subscripts W and E mean west and east, respectively. The parameter exchange procedure is executed in each iteration.

4. Results and discussion

Although the computational domain for a lithium−air cell is two dimensional, a one-dimensional model suffices to capture the necessary physics [11,12,22]. Equations (23)–(25) are solved in the moving mesh for Li^+, O_2, and ϕ_l, while equations (12) and (14) are solved in the fixed coordinate for Li_2O_2 and ϕ_s. Finite volume method is used for numerical modeling of Li−air battery considering moving boundary of the anode interface. Discretized algebraic equations are obtained using upwind scheme for both mass conservation and charge conservation equations [23−25]. An in house code is developed based on the algorithm presented in Fig. 4. Thomas algorithm is used to solve the tri-diagonal system of linear algebraic equations. The tolerances for the mass and charge conservation equations are 10^{-5}. Numerical simulations are performed on Intel Xeon 2.2 GHz. Simulations are carried out for both discharge and charge states.

In this study, the domain lengths for separator and cathode are 50 μm and 750 μm, respectively, while the length of the gap is a function of time and applied current density. Initial porosity for the separator and cathode are assumed as 0.73 [26]. A solution of lithium hexafluorophosphate ($LiPF_6$) in propylene carbonate/dimethoxyethane (PC/DME) is used as a model electrolyte for this study. The relevant electrochemical properties used in the simulation are presented in Table 2. The oxygen concentration is set to 3.26 mM at the right boundary of the cathode based on the

Table 1
Boundary conditions for governing equations (14), (23)–(25).

	$\xi = 0$ or $x = -\delta(t)$	$x = L_{sp}$	$x = L_{in}$
Lithium ion concentration (C_{Li^+})	$-D_{Li,eff}\frac{\partial C_{Li^+}}{\partial\xi} = \frac{aI_{load}}{F}$		$\frac{\partial C_{Li^+}}{\partial\xi} = 0$
Oxygen concentration (C_{O_2})	$\frac{\partial C_{O_2}}{\partial\xi} = 0$		$C_{O_2} = so_{O_2}C_{O_2,atm}$
Liquid phase electric potential (ϕ_l)	$-\kappa_{eff}\frac{\partial\phi_l}{\partial\xi} = I_{load}$		$\frac{\partial\phi_l}{\partial\xi} = 0$
Solid phase electric potential (ϕ_s)		$\frac{\partial\phi_s}{\partial x} = 0$	$-\sigma_{eff}\frac{\partial\phi_s}{\partial\xi} = I_{load}$

so_{O_2}: solubility of oxygen in electrolyte.
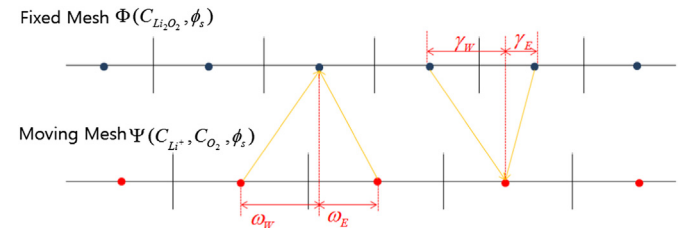
Fig. 3. Parameter mapping between fixed and moving mesh. The parameters are interpolated based on a piece-wise linear scheme.
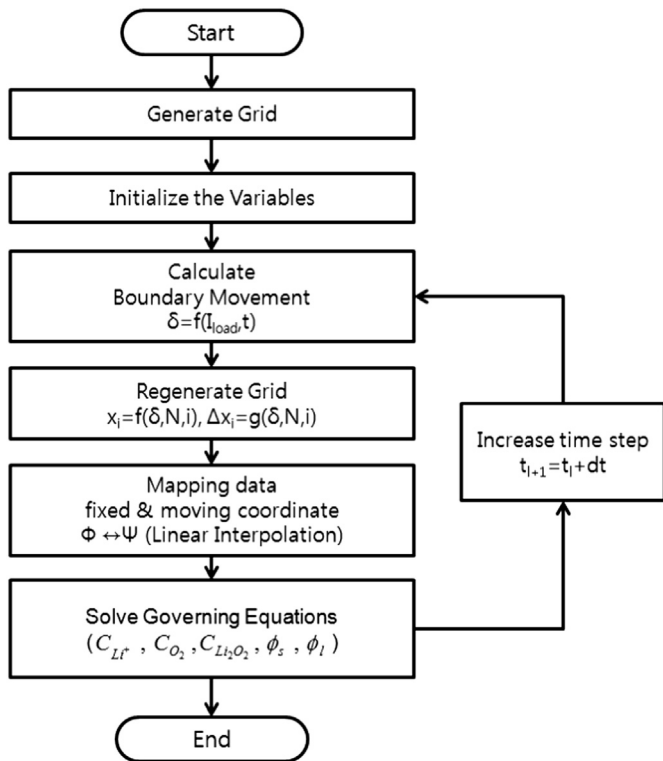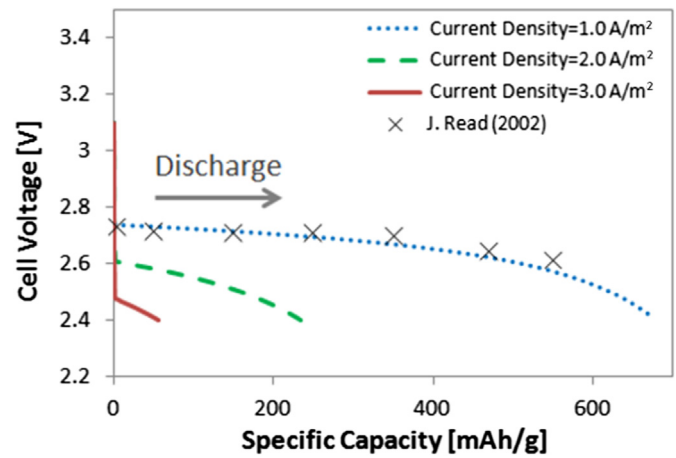
Fig. 4. An algorithm for Li–air battery simulation considering the moving anode boundary. Grid is regenerated continuously due to the movement of anode boundary.

solubility of oxygen in the electrolyte and the concentration of oxygen in the atmospheric air.

4.1. Discharge phenomena

The discharge characteristics of a lithium–air cell are shown in Fig. 5 for various current densities. Experimental data from Read [27] are also presented in Fig. 5 to compare with our simulation results. The numerical results obtained from our 1D model are in

Table 2
Parameters used in simulation.

Parameter	Value	Ref.
Electrolyte property		
Li ion diffusivity [m^2 s^{-1}]	2.11×10^{-9a}	[30,31]
Time transfer number	0.2594^a	[31]
$\partial f/\partial C_{Li}$	-1.03^a	[31]
Oxygen diffusivity [m^2 s^{-1}]	7×10^{-10a}	[32]
Oxygen solubility	0.38	[32]
Electric conductivity [S m^{-1}]	1.85	
Kinetic parameters		
Reaction rate coefficient anodic current [m s^{-1}]	1.11×10^{-15}	[12]
Reaction rate coefficient cathodic current [m^7 s^{-1} mol^{-2}]	3.4×10^{-17}	[12]
Exchange current density for anode [A m^{-2}]	1	[12]
Symmetry factor	0.5	[33]
General parameters		
Mass density of lithium peroxide [kg m^{-3}]	2140	[34]
Mass density of electrolyte solution [kg m^{-3}]	1200	[34]
Mass density of carbon [kg m^{-3}]	2260	[34]
Particle radius in the electrode [m]	25×10^{-9}	[35]
Operating temperature [K]	300	
Separator porosity	0.73	[26]
Electric parameter		
Electric conductivity of cathode [S m^{-1}]	10	[33]

[a] Concentration dependent.

Fig. 5. Voltage–capacity plot for a Li–air battery during discharge. The contribution of oxygen is not considered in the specific capacity calculation. At higher current density battery drains faster.

good agreement with existing literature, thus validating our numerical model. Here, the specific capacity is calculated based on

$$SC_{\text{dis}} = \int_0^t \frac{A \cdot I_{\text{load}}}{(1 - \varepsilon_0)\rho_{ca}\overline{V}}dt \tag{33}$$

where I_{load}, A, $\overline{V}$, ε_0, and ρ_{ca} are current density during discharge, anode surface area, bulk cathode volume, initial cathode porosity, and initial cathode weight density, respectively. It is important to note that in equation (33) the transient change in cathode porosity and density are not taken into consideration. In other words, specific capacity is just a linear function of operating time. That means, for higher current density of a load, the battery will be discharged quickly, which is expected like any other battery.

Simulation results indicate (Fig. 5) that the cell voltage drops with time. The potential drop is very sharp at the beginning at which the cell voltage drops from the open circuit potential (3.1 V) due to kinetic losses [28]. The kinetic losses worsen as the current density of the load is increased. Fig. 5 also reveals that the potential drops linearly after the initiation period, but it decays exponentially near the specific capacity limit [28]. There are two possible explanations for this exponential potential drop. The first one comes from the blocking of porous region in the cathode as discharge continues. The cathode porosity is decreased due to buildup of Li$_2$O$_2$ deposit. Fig. 6(a) shows the porosity distribution with time and location. The porosity remains constant in the gap and separator, but changes in the cathode region because of the reduction reaction only at the porous space within cathode. The porosity drops at a faster pace in the right side of the cathode than any other location in the cathode. In other words, the pore blocking problem due to lithium peroxide deposition is more serious near oxygen feed side in the cathode, and this problem is well documented in experimental work [27].

The porosity distribution in the cathode region can also be explained from the oxygen concentration (Fig. 6(b)). During the discharge process, oxygen transport takes place from the atmospheric side to the separator due to existence of a concentration gradient. This gradient implies that the highest concentration of oxygen occurs at the right side of the cathode, and the oxygen concentration decreases inward. The higher availability of oxygen in the atmospheric side will cause higher reaction rate and higher transfer current in the atmospheric side as shown in Fig. 6(c), which

is responsible for production of more lithium peroxide deposit in the right side of the cathode. As the deposition of Li$_2$O$_2$ continues, the flow of oxygen towards separator decreases due to physical blocking and reduction of the effective diffusivity of oxygen in the right (source) side of the cathode. For instance, the effective diffusivity of oxygen is reduced to one third of its initial value as cathode porosity is reduced to 0.4 from 0.73. This reduction in porosity causes overall decrease in oxygen concentration at the left side of the cathode as discharge continues. At one point, oxygen gets completely depleted at the left boundary of the cathode, and this depletion zone continues to extend towards the right side (Fig. 6(b)). In the oxygen depleted zone, reduction reaction does not occur and this zone is called the "dead zone". The dead zone is also evident from transfer current value presented in Fig. 6(c). The transfer current approaches zero in oxygen depleted zone and, consequently, the reaction area is decreased causing very high cell voltage drop at the specific capacity limit.

The second reason for the cell potential drop is related to electric passivation due to lithium peroxide formation. As the thickness of the lithium peroxide deposit increases, the film resistance (R_{film}) increases which will increase the $\Delta\phi_{film}$ causing a net negative effect on the cell potential. The relative influence of electric passivation on cell potential drop is higher than that of oxygen limitation as shown in Fig. 7. This result is in agreement with the work of Albertus et al. [28]. Our numerical results indicate that the cell voltage drop is linear for oxygen limited case, while it drops exponentially when the cell's performance is limited by the electric passivation. Nevertheless, the oxygen limitation is still a noticeable factor on the overall cell voltage drop as shown in the combined plot (Fig. 7).

4.2. Charge phenomena

The charge characteristics of a lithium–air cell are shown in Fig. 8 for various applied current densities. Like discharge case, the experimental results from Read [27] are also presented for 1.0 A m^{-2} applied current density, and a very good agreement between experiments and modeling results are obtained. During charging of the battery, the specific capacity is calculated from

$$SC_{ch} = SC_{dis}(t = t_d) + \int_{t_d}^{t} \frac{A \cdot I_{load}}{(1 - \varepsilon_0)\rho_{ca} \overline{V}} dt \qquad (34)$$

where t_d is the end of discharge time. The current density becomes negative during charge. Thus, specific capacity decreases with
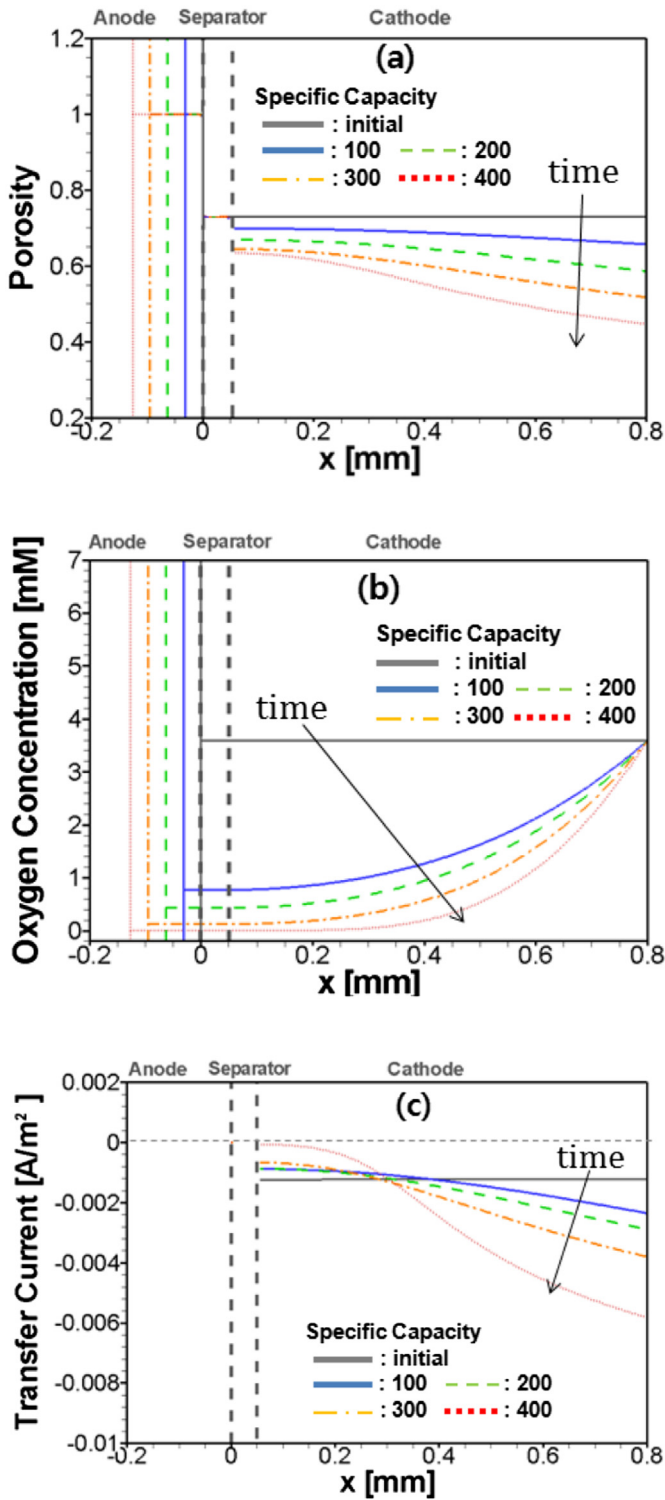

Fig. 6. Spatial distribution of (a) porosity, (b) oxygen concentration, and (c) transfer current density during discharge state for current density of 1A m^{-2}. Anode reaction plane moves left during discharge. The transfer current is due to transport of ions. Negative transfer current density means reduction reaction, while positive transfer current density means oxidation reaction.
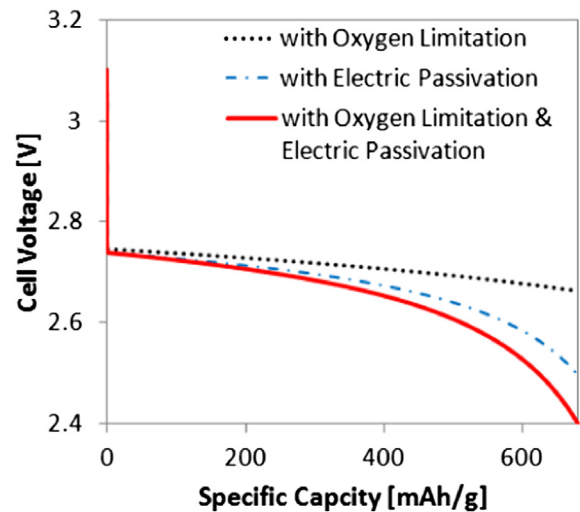

Fig. 7. Cell electric performance with and without oxygen limitation and electric passivation. All other simulation conditions are same as Fig. 6.
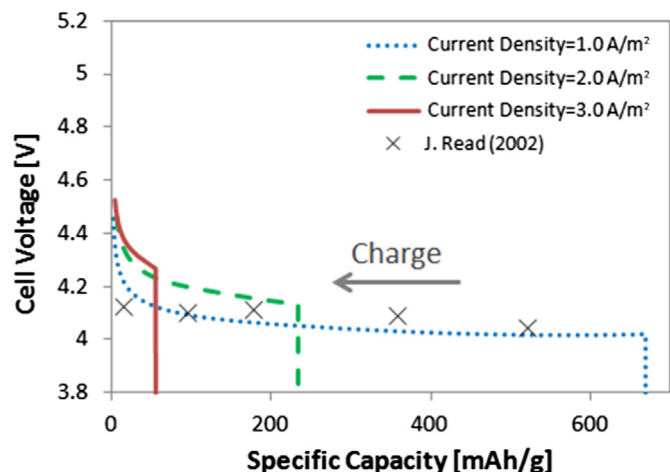
Fig. 8. Voltage–capacity plot for a Li–air battery during discharge. The contribution of oxygen is not considered in the specific capacity calculation. At higher current density battery gets charged quickly.

charging time. In other words, the battery will be fully charged when the specific capacity approaches zero. It is important to note that the effect of oxygen mass is not considered in the conventional specific capacity presented in equation (34).

As expected, at the beginning of the charging state ($t \to t_d$) the cell voltage sharply jumps above the open circuit potential. After that sudden change, the cell potential continue to rise at a slower rate during the charging phase, but increases exponentially once the battery is almost charged ($SC_{ch} \to 0$). This exponential change in potential is due to diminution of cathode reaction space which is discussed later. Fig. 8 also reveals that the specific capacity decreases significantly for higher applied current density, indicating shorter time for charging. Although shorter charging period is very desirable for both auto industry and consumer electronics, the high current density can affect the lithium anode morphology adversely. Cohen et al. [29] demonstrated dendrite formation at the anode interface at higher applied current density. These dendrites might block the electrolyte flow at the anode reaction interface. In addition, these dendrites can cause structural damage in the separator resulting in internal short.

Fig. 9 shows the spatial distribution of various parameters during the charging phase. In this case, cathode acts like an oxygen source, where oxygen is produced from the oxidation of lithium peroxide and is released to atmosphere. Thus, the concentration of oxygen is higher at the left side of the cathode and it reaches to the atmospheric level at the right boundary of the cathode (Fig. 9(a) and (b)). For an ideal system, the maximum oxygen concentration would be 10 mM if there is no oxygen solubility limitation (Fig. 9(a)). However, in an organic electrolyte, the maximum concentration of solvated oxygen is generally 5 mM or less because of solubility limitation. Thus, it is assumed that the maximum oxygen concentration in the solvated (liquid) phase is 5 mM (Fig. 9(b)) and the rest of oxygen is emitted to the atmosphere in the gas phase. The total value of oxygen concentration reduces with time because reaction region in the cathodic side decreases. However, the concentration of solvated oxygen remains almost constant during the early phase of charging, and goes down close to the fully charged state (Fig. 9(b)).

Fig. 9(c) shows the porosity distribution in the cathode side. As time progresses, the region with lithium peroxide shrinks and results in higher porosity in cathode. At the fully charged state, the porosity fully recovers to its initial value. The depletion of lithium peroxide takes place quickly in the left side compared to the right

side of the cathode. This is due to the fact that at the end of the discharge state lesser amount of lithium peroxide is available in the left side of the cathode compared to the right side. Near the completion of the charge state, lithium peroxide deposits are completely depleted at the left side of the cathode. This results in zero current density from that area due to the lack of oxidation reaction (Fig. 9(d)) near cathode-separator interface. Thus, for a constant applied current density, the transfer current increases at the right side of the cathode causing very high cell voltage near the completion of the charge state. During the charge state, the gap between separator and anode is reduced due to recovery of lithium at the anode, and ideally the separator will touch the metallic anode at the end of the charge state.

4.3. Effect of volume change

In a metal anode cell, the available space for electrolyte changes due to the movement of anode interface and changes in cathode porosity. During the discharge state, gap between separator and anode is increased while cathode porous area is decreased. So, the total available space is a function of time. If the lithium peroxide is insoluble in the electrolyte, the available space for electrolyte in the cathode region will decrease by the amount of lithium peroxide produced. On the other hand, if lithium peroxide is totally soluble, the porous space in cathode is maintained and, consequently, total available space for electrolyte would increase.

Fig. 10 shows the ratio of available volume to the initial volume of the electrolyte for discharge. In this study, this ratio was obtained by substituting equations (19) and (26) into (27) as

$$r(t) = \frac{A}{V_{el}}\left[\frac{M_{Li}}{\nu_{Li}\rho_{Li}F}\int_0^t (I_{load})dt + \varepsilon_{sp}L_{sp}\right] + \frac{A}{V_{el}}\int_{L_{sp}}^{L_{sp}+L_c}\varepsilon_c(t)dx \quad (35)$$

The calculation of the first two terms of equation (35) is straight forward. But the third term requires special attention since the porosity of the cathode region changes with time. One can easily find this time dependent porosity change from numerical results. In this study, we calculated the third term from an analytical model. The porous volume of the cathode can be calculated by subtracting the space occupied by the Li$_2$O$_2$ from the initial cathode porous volume as

$$A\int_{L_{sp}}^{L_{sp}+L_c}\varepsilon_c(t)dx = AL_c\varepsilon_c(0) - A\frac{M_{Li_2O_2}}{2\rho_{Li_2O_2}F}\int_0^t (I_{load})dt \quad (36)$$

where $M_{Li_2O_2}$ and $\rho_{Li_2O_2}$ are molecular weight and density of lithium peroxide, respectively.

The aforementioned analytical model shows that the ratio decreases with increase in specific capacity if lithium peroxide is insoluble, but it increases if lithium peroxide is soluble. If lithium peroxide is soluble in electrolyte, the battery performance will be enhanced due to elimination of electrical passivation effect [28] discussed later. On the other hand, if the lithium peroxide is insoluble in electrolyte, electrolyte leakage can happen due to decrease of total available space for electrolyte. The amount of electrolyte leakage, estimated from simulation, is presented in Table 3. Generally, electrolyte leakage is serious when the applied current density is low because of high specific capacity (Fig. 5), which eventually ruins a battery.

Next, we study the performance of a lithium–air battery considering variable level of solubility of lithium peroxide. Fig. 11 shows the voltage–capacity curve during discharge for a current
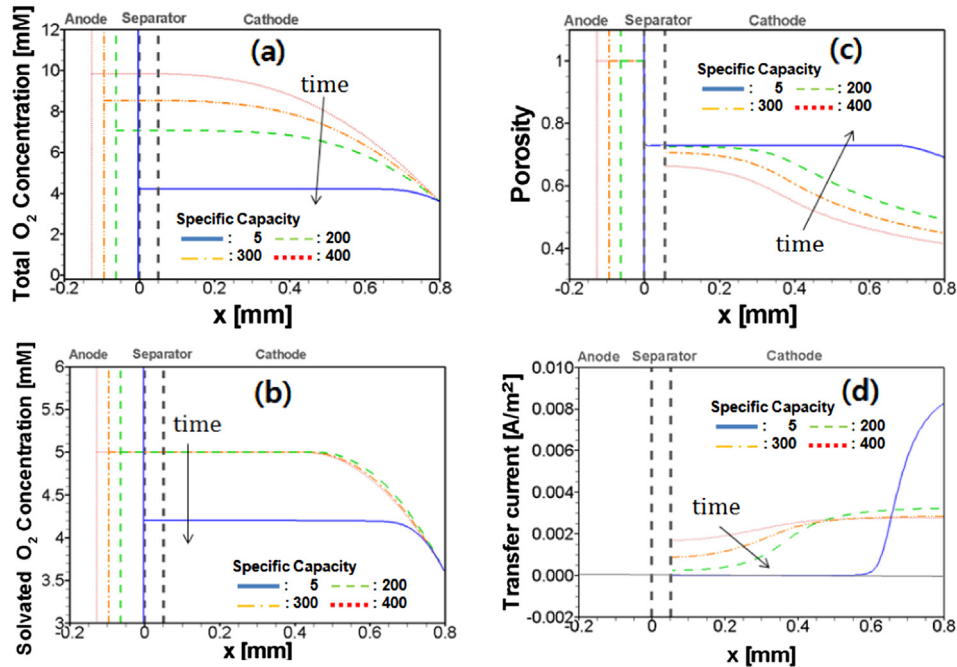
Fig. 9. Spatial distribution of (a) total oxygen concentration, (b) solvated oxygen concentration, (c) porosity, and (d) transfer current density during charge state for current density of 1 A m^{-2}. Anode reaction plane moves towards right during charging, and the anode will touch the separator at the end of the charging process.

density of 1 A m^{-2}. The cell voltage drop due to passivation is significant when lithium peroxide is insoluble. On the other hand, for a completely soluble case, the performance of a lithium–air battery can be improved significantly due to elimination of the passivation effect. The numerical model predicts a constant cell potential in a totally soluble case, and this result supports the findings of Albertus et al. [28]. However, in reality it is impossible to maintain constant cell voltage for a very long period of time, and it will continue to drop with time. There are two possible explanations for deviation from this ideal case (constant cell potential). First, the lithium peroxide cannot be completely dissolved in the electrolyte. Second, there is a change in the effective reaction surface area at the anode interface when lithium peroxide is partially or totally soluble in the electrolyte. For that reason, the cell potential drops with time even for completely soluble lithium peroxide if the effective reaction area is considered in the voltage–

capacity study. The effect of change in reaction area is even more significant when passivation is considered (blue line). Therefore, it can be concluded that the cell voltage cannot be maintained constant due to the change in effective reaction area even if electrical passivation is totally eliminated with proper design and selection of electrolytes.

5. Conclusions

A mathematical model is developed for Li–air batteries considering changes in volume as well as effective reaction area in both anodic and cathodic sides. Governing equations are developed for transport of lithium ion and oxygen as well as for liquid phase electric potential using the moving coordinate system. These aforementioned governing equations are solved in moving mesh, while governing equations for lithium peroxide and solid phase electric potential are solved only in the fixed cathode region. The results from this model are validated with existing experimental results.

Electrical performance of a lithium–air battery is predicted for various load conditions for both discharge and charge states. During discharge, a gap is formed between the separator and anode which is filled with the electrolyte enabling transfer of lithium ions from anode to cathode. Also, during discharge, lithium peroxide is formed in the cathode porous space causing passivation of the cathode. The cell potential changes gradually during the regular operation range because of decrease in the active cathode area for reduction reaction. The consequence of this is lower porosity in the cathode, which inhibits the oxygen flow further causing dead zone near the separator. The dead zone grows significantly at the specific
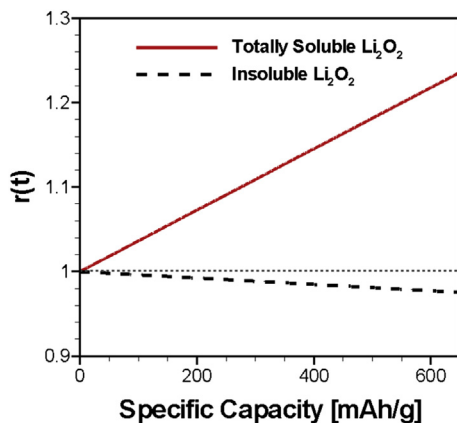
Fig. 10. The ratio of available volume for electrolyte to the initial electrolyte volume for different solubility of lithium peroxide during discharge. All other simulation conditions are same as Fig. 6.

Table 3
Percentage of electrolyte leakage for an applied current density of 1 A m^{-2}.

Specific capacity [mAh g^{-1}]	100	200	300	650
Leakage [%]	0.40	0.70	1.09	2.15
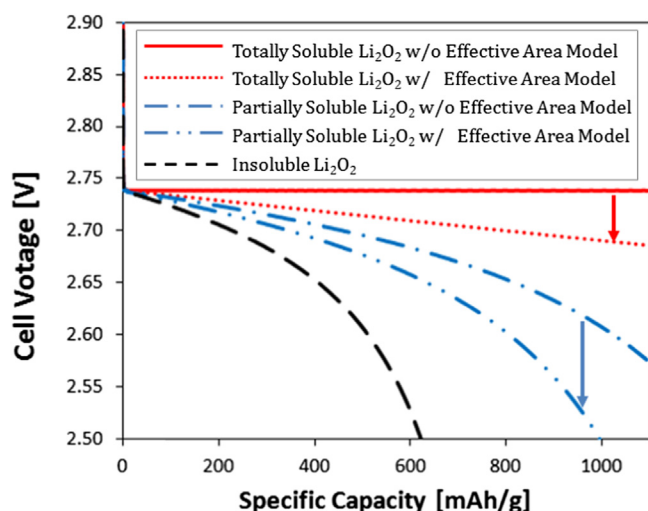
Fig. 11. Voltage–capacity curves for different level of lithium peroxide solubility in the electrolyte. There is a significant difference between the performance results if the effective reaction area is taken into consideration due to the volume change.

capacity limit and results in steep drop in cell voltage as well as performance. On the other hand, during charge, the gap between the anode interface and separator decreases with time due to the recovery of metallic lithium in the anode. Like in the case of discharge, the dead zone is first formed at the interface of separator and the cathode because of the depletion of lithium peroxide. This dead zone continues to move towards the atmospheric side of the cathode.

During charging state, the oxygen concentration is highest at the interface between separator and cathode, and it decreases towards the atmospheric side. For the system shown in this study, the total concentration of oxygen is higher than the maximum permissible oxygen concentration in an organic electrolyte. The excess oxygen has to leave the system in gas phase which might block the porous structure due to the formation of bubbles. This bubble formation might be prevented by developing electrolytes with higher oxygen solubility.

This numerical study shows that the effective reaction area as well as the volume available for electrolyte changes during discharge and charge operation. These changes strongly depend on the solubility of lithium peroxide in electrolyte in the cathode region. For totally soluble lithium peroxide in an electrolyte, the available electrolyte volume increases (decreases) with time for discharge (charge). Numerical results further reveal that the cell

voltage cannot be maintained constant because of reduction of effective reaction area.

Acknowledgments

References

[1] E.J. Cairns, P. Albertus, Batteries for Electric and Hybrid-Electric Vehicles, in: J.M.D.M.F.S.M.A. Prausnitz (Ed.), Annual Review of Chemical and Biomolecular Engineering, vol. 1, 2010, pp. 299–320.
[2] J.-S. Lee, S.T. Kim, R. Cao, N.-S. Choi, M. Liu, K.T. Lee, J. Cho, Adv. Energy Mater. 1 (2011) 34–50.
[3] G. Girishkumar, B. McCloskey, A.C. Luntz, S. Swanson, W. Wilcke, J. Phys. Chem. Lett. 1 (2010) 2193–2203.
[4] P.G. Bruce, S.A. Freunberger, L.J. Hardwick, J.M. Tarascon, Nat. Mater. 11 (2012) 19–29.
[5] M. Doyle, T.F. Fuller, J. Newman, J. Electrochem. Soc. 140 (1993) 1526–1533.
[6] C.Y. Wang, W.B. Gu, B.Y. Liaw, J. Electrochem. Soc. 145 (1998) 3407–3417.
[7] P.M. Gomadam, J.W. Weidner, R.A. Dougal, R.E. White, J. Power Sources 110 (2002) 267–284.
[8] J.S. Newman, Electrochemical Systems, Prentice-Hall, Englewood Cliffs, N.J., 1972.
[9] J.T.W. Newman, AIChE J. 21 (1975) 25–41.
[10] J. Newman, K.E. Thomas, H. Hafezi, D.R. Wheeler, J. Power Sources 119 (2003) 838–843.
[11] S.S. Sandhu, J.P. Fellner, G.W. Brutchen, J. Power Sources 164 (2007) 365–371.
[12] U. Sahapatsombut, H. Cheng, K. Scott, J. Power Sources 227 (2013) 243–253.
[13] J. Christensen, P. Albertus, R.S. Sanchez-Carrera, T. Lohmann, B. Kozinsky, R. Liedtke, J. Ahmed, A. Kojic, J. Electrochem. Soc. 159 (2012) R1–R30.
[14] M. Winter, J.O. Besenhard, Electrochim. Acta 45 (1999) 31–50.
[15] B. Scrosati, J. Garche, J. Power Sources 195 (2010) 2419–2430.
[16] S.J. Visco, Y.S. Nimon, L.C.D. Jonghe, B.D. Katz, A. Petrov, US Patent, 7,824,806 B2, 2010.
[18] E. Peled, D. Golodnitsky, G. Ardel, J. Electrochem. Soc. 144 (1997) L208–L210.
[19] S.S. Zhang, D. Foster, J. Read, J. Power Sources 195 (2010) 1235–1240.
[20] D.A.G. Bruggeman, Ann. Phys. 24 (1935) 636–679.
[21] G.F. Carey, Computational Grids: Generation, Adaptation, and Solution Strategies, Taylor & Francis, Washington, D.C., 1997.
[22] Y. Wang, Electrochim. Acta 75 (2012) 239–246.
[23] J. Shim, P. Dutta, C. Ivory, Numer. Heat Transfer A: Appl. 52 (2007) 441–461.
[24] I.B. Sprague, D. Byun, P. Dutta, Electrochim. Acta 55 (2010) 8579–8589.
[25] I. Sprague, P. Dutta, Numer. Heat Transfer A: Appl. 59 (2011) 1–27.
[26] Y.-C. Lu, D.G. Kwabi, K.P.C. Yao, J.R. Harding, J. Zhou, L. Zuin, Y. Shao-Horn, Energy Environ. Sci. 4 (2011) 2999–3007.
[27] J. Read, J. Electrochem. Soc. 149 (2002) A1190–A1195.
[28] P. Albertus, G. Girishkumar, B. McCloskey, R.S. Sanchez-Carrera, B. Kozinsky, J. Christensen, A.C. Luntz, J. Electrochem. Soc. 158 (2011) A343–A351.
[29] Y.S. Cohen, Y. Cohen, D. Aurbach, J. Phys. Chem. B 104 (2000) 12282–12291.
[30] S.G. Stewart, J. Newman, J. Electrochem. Soc. 155 (2008) F13–F16.
[31] A. Nyman, M. Behm, G. Lindbergh, Electrochim. Acta 53 (2008) 6356–6365.
[32] J. Read, K. Mutolo, M. Ervin, W. Behl, J. Wolfenstine, A. Driedger, D. Foster, J. Electrochem. Soc. 150 (2003) A1351–A1356.
[33] P. Andrei, J.P. Zheng, M. Hendrickson, E.J. Plichta, J. Electrochem. Soc. 157 (2010) A1287–A1295.
[34] F. Macdonald, Abstr. Pap. Am. Chem. Soc. 238 (2009).
[35] H. Cheng, K. Scott, J. Power Sources 195 (2010) 1370–1374.